Physiological flexibility of phytoplankton impacts modeled biomass and primary production across the North Pacific Ocean

Yoshikazu Sasai[1], Sherwood Lan Smith[1], Eko Siswanto[2], Hideharu Sasaki[3], and Masami Nonaka[3]

[1]Earth Surface System Research Center (ESS), Research Institute for Global Change (RIGC), Japan Agency for Marine-Earth Science and Technology (JAMSTEC), Yokosuka, Japan
[2]ESS,RIGC,JAMSTEC,Yokohama,Japan
[3]Application Laboratory (APL), Research Institute for Value - Added - Information Generation (VAiG), JAMSTEC, Yokohama, Japan

Correspondence: Yoshikazu Sasai (ysasai@jamstec.go.jp)

Abstract. Phytoplankton growth, and hence biomass responds to changing light and nutrient conditions in the near-surface ocean. Although a wide variety of physiological photoacclimation models have been developed and tested against laboratory results, their application and testing against oceanic observations remain limited. Hence the biogeochemical implications of photoacclimation in combination with ocean circulation have yet to be fully explored. We compare modeled phytoplankton
5 biomass and primary production from a recently developed flexible phytoplankton functional type model (FlexPFT), which incorporates photoacclimation and variable carbon (C):nitrogen (N):chlorophyll (Chl) ratios, to that obtained with an inflexible control model (InFlexPFT), which assumes fixed C:N:Chl ratios. We couple each plankton model with a 3-D eddy-resolving ocean circulation model of the North Pacific and evaluate their respective performance versus observations of Chl, nutrients, and primary production. These two models yield different horizontal and vertical distributions of Chl and primary production.
10 The FlexPFT reproduces observed subsurface Chl maxima, although it overestimates Chl concentrations. In the subtropical gyre, where light is sufficient, even at low nutrient concentrations, the FlexPFT yields faster growth rates, as well as high Chl concentration and primary production in the subsurface layer. Compared to the FlexPFT, the InFlexPFT yields slower growth rates, and lower Chl and primary production. In the subpolar gyre, the FlexPFT also predicts faster growth near the surface, where light and nutrient conditions are most favorable. Compared to the InFlexPFT, the key differences that allow the FlexPFT
15 to better reproduce the observed patterns are its assumption of variable, rather than fixed, C:N:Chl ratios and inter-dependent, rather than strictly multiplicative, effects of light- and nutrient-limitation.

1 Introduction

20 Marine phytoplankton carry out approximately half of global primary production (Field et al., 1998) and sustain the marine food web. Much effort has therefore been expended to understand and develop predictive models of phytoplankton growth and associated marine ecosystem processes and biogeochemistry. Phytoplankton models have for decades been constructed by combining various empirically-based formulations for different physiological processes, such as photosynthesis as a function of irradiance, growth as a function of nutrient availability, and the regulation of chlorophyll (Chl) content and cellular compo-

25 sition, which is termed photoacclimation (e.g., Platt and Jassby, 1976; Droop, 1983; Geider et al., 1998; Baklouti et al., 2006). Various formulations have been derived from laboratory experiments and in-situ observations, typically for the response of a single key process (e.g. nutrient uptake or growth rate) to one or a few key environmental variables (e.g., nutrient concentration, light intensity, temperature). Global ocean biogeochemical models require combining multiple processes with sufficient generality to apply over a wide range of environmental conditions. This formidable challenge can be approached in various

30 ways, which are still debated (e.g., Flynn, 2003, 2010; Franks, 2009; Anderson, 2010; Smith et al., 2016).

Most phytoplankton models as used in global ocean biogeochemical models (e.g., Follows et al., 2007; Totterdell, 2019), apply the Monod equation (Monod, 1949) for phytoplankton growth as a function of ambient nutrient concentration and assume fixed stoichiometry between carbon and nutrients in phytoplankton and organic matter (Redfield et al., 1963) for the sake

35 of computational efficiency and simplicity. However, the actual elemental composition of phytoplankton and organic matter varies depending on environmental conditions (e.g., Smith et al., 1992; Martiny et al., 2013; Garcia et al., 2018b; Liefer et al., 2019). In general, phytoplankton can sustain relatively high growth rates even when nutrient uptake rates are severely substrate-limited, by producing biomass containing less of whatever required elements are in short supply (Flynn, 2010). Phytoplankton grow with carbon, C: nitrogen, N ratios higher than the Redfield ratio when N is limiting and lower than the Redfield ratio when

40 light is limiting (e.g., Goldman et al., 1979; Falkowski et al., 1985; Smith et al., 1992). The inability of the Monod equation to describe adequately laboratory experiments and in-situ observations for the dependence of growth rate on nutrient concentration led to the development of the Droop quota model (Droop, 1968, 1983). The Droop quota model for growth explicitly accounts for flexible stoichiometry by including independent state variables for carbon and nutrient biomasses with separate functions for acquiring each element (Caperon, 1968; Droop, 1968). Because the flexible stoichiometry of phytoplankton links

45 phytoplankton growth to biogeochemical cycles, the model has been applied to 1-dimensional (1-D) and 3-dimensional (3-D) ocean biogeochemical models and proved useful to account for observations of the composition of phytoplankton and organic matter (e.g., Moore et al., 2001; Vichi et al., 2007; Ayata et al., 2013; Ward et al., 2013). However, the application of such detailed models at the global scale has been restricted by both practical considerations of their computational requirements and scientific concerns about increased complexity (e.g., a greater number of parameters values and processes) relative to simpler

50 fixed stoichiometry models.

Recently, as a potential solution to this problem, Smith et al. (2016) derived a computationally efficient Instantaneous Acclimation (IA) approach, which represents flexible phytoplankton composition, similar to the Droop quota model, but without introducing additional state variables for each element or pigment considered. This "Flexible Phytoplankton Functional Type"
55 (FlexPFT) model accounts for the adaptive response to changing light and nutrient conditions in terms of two trade-offs for allocation of intracellular response: (i) carbon versus nitrogen assimilation (Pahlow and Oschlies, 2013), and (ii) affinity for nutrient versus maximum uptake rate (Pahlow, 2005; Smith et al., 2009). Smith et al. (2016) applied the FlexPFT model in a 0-D setup, and assessed its performance in terms of phytoplankton seasonality, including variable composition for changing light and nutrient conditions, at two observation sites (Station K2, 47°N, 160°E, and Station S1, 30°N, 145°E) in the North
60 Pacific. Ward (2017) further tested this approach and suggested that it has promise for incorporating flexible stoichiometry into global ocean biogeochemical models. Kerimoglu et al. (2021) further assessed the performance of the IA approach, as compared to the typical assumption of fixed stoichiometry, in an idealized setup capturing typical seasonal variations of environmental conditions in a 1-D water column, accounting for the coupling of phytoplankton growth and biogeochemistry with physical transport by advection and diffusion. Anugerahanti et al. (2021) assessed the performance of the IA approach
65 favorably compared to a suite of models of differing complexity, based on comparisons of 1-D model performance against extensive time-series observations from subtropical stations ALOHA (A Long term Oligotrophic Habitat Assessment, 22.45°N, 158°W) in the North Pacific and BATS (Bermuda Atlantic Time Series, 31.67°N, 64.167°W) in the North Atlantic. Masuda et al. (2021) applied the FlexPFT model in a global 3-D setup and showed that it could reproduce the global distribution of observed subsurface chlorophyll maxima (SCM). However, for 3-D applications, especially with global ocean biogeochemical
70 models and earth system models, the challenge remains to reproduce the large-scale ocean conditions with computational efficiency and minimal tuning of model parameters. In this context, only limited tests have so far been conducted against oceanic observations. Here we explore the biogeochemical implications of the IA approach and the eco-physiological assumptions underlying the FlexPFT model in combination with large-scale ocean circulation.

75 To evaluate the adaptive response of phytoplankton growth to the varying light and nutrient conditions across the North Pacific, we compare modeled phytoplankton biomass and production from a recently developed phytoplankton model (FlexPFT, Smith et al., 2016), which incorporates photoacclimation and variable C:N:Chl, to that obtained with an inflexible control (InFlexPFT) model, which is a typical Nitrate-Phytoplankton-Zooplankton-Detritus (NPZD) type model (Sasai et al., 2006, 2010, 2016) assuming fixed C:N:Chl ratios (fixed stoichiometry). We apply these two phytoplankton models (FlexPFT and InFlexPFT) in a
80 3-D eddy-resolving ocean circulation model of the North Pacific, namely the Ocean general circulation model For the Earth Simulator (OFES2, Sasaki et al., 2020), to assess each model's performance.

2 Methods and Materials

2.1 The Coupled Physical-Biological Model

85   We used an eddy-resolving (1/10°) coupled physical-biological model of the North Pacific, consisting of the OFES2 including sea-ice (Masumoto et al., 2004; Komori et al., 2005; Sasaki et al., 2020) coupled with a simple nitrogen-based NPZD pelagic model (Sasai et al., 2006, 2010, 2016). The OFES2 domain extends from 20°S in the South Pacific to 68°N in the North Pacific and from 100°E to 70°W. The model has 1/10° horizontal resolution with 105 vertical levels, from 5 m thickness at the surface to 300 m thickness at the maximum depth of 7500 m. The physical fields were spun up under climatological forcing data (wind

90   stresses, heat flux, and freshwater flux) from the Japanese 55-year Reanalysis (JRA55-do) (Tsujino et al., 2018) and observed climatological fields of temperature and salinity (World Ocean Atlas 2009, WOA09) (Antonov et al., 2010; Locarnini et al., 2010) without motion for 50 years. After 50 years of spin-up integration, the OFES2 was forced by 3-hourly JRA55-do from 1958 to 1979. The last day of 1979 is used for the initial physical fields for the simulation.

95   In the OFES2, an advection-diffusion equation, Eq. A1 (Appendix A), is used to calculate the evolution of four biological tracer concentrations (nitrogen-based units, mmol N m^{-3}): Nitrogen, N, Phytoplankton, P, Zooplankton, Z, and Detritus, D. The source and sink terms represent the biological activity (Eqs. A2 - A5) as described by Sasai et al. (2006, 2010, 2016). In this study, to examine how the physiological flexibility of phytoplankton impacts modeled biomass and primary production (PP), two phytoplankton models (FlexPFT and InFlexPFT), respectively, are applied for the phytoplankton growth term, μP,

100   in the Eq. A2. The remaining biological activity equations and biological parameters (e.g., Grazing, Mortalities of P and Z, and Decomposition of D) are the same for both models (Appendix A). The initial nitrogen N (mmol N m^{-3}) field is taken from the WOA09 (Garcia et al., 2010). The initial phytoplankton and zooplankton concentrations are set to 0.2 mmol N m^{-3} at the sea surface, decreasing exponentially with an e-folding scale depth of 100 m. Detritus is initialized to 0.1 mmol N m^{-3} everywhere. Two NPZD models are incorporated after the last day of 1979 of the OFES2. The two coupled physical-biological

105   models are forced by 3-hourly JRA55-do from 1980 to 2019.

2.2 Formulations of Phytoplankton Growth

Here, we briefly describe the two phytoplankton growth rate equations, FlexPFT and InFlexPFT, used in this study, which appear in the first term of the right-hand side, μP, in Eq. A2. In both models, phytoplankton growth rate, μ (day^{-1}), depends

110   on irradiance, I, which is the intensity of photosynthetically active radiation calculated from daily mean shortwave radiation (W m^{-3}) of JRA55-do, nitrogen, N (mmol N m^{-3}), and temperature, T (°C). N and T are used from the coupled physical-biological models' output. The FlexPFT growth rate, $\mu_{Flex}(N, I, T)$ (day^{-1}) (Smith et al., 2016) is:

$$\mu_{Flex}(N, I, T) = \mu_{max} \left(1 - \frac{Q_s}{Q} - f_V \right) S(I, T) F(T) \tag{1}$$

where μ_{max} is the potential maximum growth rate (day^{-1}), Q_s is the structural minimum cell quota (mol N (mol C)$^{-1}$) given

115 as a fixed parameter (= $Q_0/2$, where $Q_0(= 0.039)$ is the minimum cell quota, Edwards et al., 2012), Q is the nitrogen cell quota, i.e. the intracellular N content per unit carbon biomass (mol N (mol C)$^{-1}$) as a function of I, N, and T, and f_V is the fractional allocation of intracellular resources to nutrient uptake (dimensionless) as defined by Pahlow et al. (2013). The cell quota, Q, is:

$$Q = Q_s \left[1 + \sqrt{1 + \left[Q_s \left(\frac{\mu_{Flex}(I,T)}{\hat{V}^N(N,T)} + \zeta^N \right) \right]^{-1}} \right] \tag{2}$$

120 where $\mu_{Flex}(I,T)(= \mu_{max}S(I,T)F(T))$ is growth rate as a function of μ_{max}, I, and T, $\hat{V}^N(N,T)$ is potential nutrient uptake rate, and ζ^N is the energetic respiratory cost of assimilating inorganic nitrogen (0.6 mol C (mol N)$^{-1}$, Pahlow and Oschlies, 2013). The potential nutrient uptake rate, $\hat{V}^N(N,T)$, is:

$$\hat{V}^N(N,T) = \frac{\hat{V}_0 N}{N + \left(\frac{\hat{V}_0}{\hat{A}_0} \right) + 2\sqrt{\left(\frac{\hat{V}_0 N}{\hat{A}_0} \right)}} \tag{3}$$

where $\hat{V}_0$ and $\hat{A}_0$ are the potential maximum uptake rate for N (day^{-1}) and the potential maximum affinity for N (m^3 (mmol

125 N)$^{-1}$ day^{-1}). The fractional allocation of intracellular resources to nutrient uptake, f_V, as defined by Pahlow et al. (2013) is:

$$f_V = \frac{\mu_{Flex}(I,T)}{\hat{V}^N(N,T)} \left[-1 + \sqrt{1 + \left[Q_s \left(\frac{\mu_{Flex}(I,T)}{\hat{V}^N(N,T)} + \zeta^N \right) \right]^{-1}} \right] \tag{4}$$

$S(I,T)$ specifies the dependence on I (Pahlow et al., 2013), and $F(T)$ is Arrhenius-type temperature dependence. $S(I,T)$ and $F(T)$ are defined as, respectively:

$$S(I,T) = 1 - exp \left\{ \frac{-\alpha\hat{\theta}I}{\mu_{max}F(T)} \right\} \tag{5}$$

130 $$F(T) = exp \left\{ \frac{-E_a}{R} \left[\frac{1}{T + 298} - \frac{1}{T_{ref} + 298} \right] \right\} \tag{6}$$

here α is the Chl-specific initial slope of growth versus light intensity (dimensionless), and $\hat{\theta}$ is the Chl:C ratio (g chl (mol C)$^{-1}$) of the chloroplast, as described by Pahlow et al. (2013). E_a is the activation energy (4.8 × 10^4 J mol^{-1}), R is the gas constant (8.3145 J (mol K)$^{-1}$), and T_{ref} is the reference temperature (taken as 20°C).

135   The InFlexPFT for growth rate, $\mu_{InFlex}(N,I,T)$ (day^{-1}), is based on the Optimal Uptake kinetics equation (Smith et al.,
2009):

$$\mu_{InFlex}(N,I,T) = \mu_{max} \left(\frac{N}{N + \left(\frac{\hat{V}_0}{\hat{A}_0} \right) + 2\sqrt{\frac{\hat{V}_0 N}{\hat{A}_0}}} \right) S(I,T)F(T) \qquad (7)$$

where $\hat{V}_0$ is the potential maximum uptake rate for N (day^{-1}), and $\hat{A}_0$ is the potential maximum affinity for N (m^3 (mmol
N)$^{-1}$ day^{-1}), following the Optimal Uptake equation (Smith et al., 2009, 2010). Compared to the Monod equation for growth

140   as a function of ambient nutrient concentration, as typically applied in fixed composition models, this equation yields a similar
response, but with a slightly flatter shape (Smith et al., 2009). Its use here ensures that the inflexible control model has the same
nutrient uptake response as the FlexPFT, so that the only differences between the two models are the trade-off between light and
nutrient acquisition (f_V) and the variable Chl:C ratios, which are only included in the FlexPFT. In the InFlexPFT the Chl:C
ratio, which appears in the light limitation term $S(I,T)$ (Eq. 5), is set to a constant value ($\hat{\theta} = 0.6$). The same temperature

145   dependence, $F(T)$, is assumed in both models. Parameter values (Table 1) used in Eqs. 1 to 7 for the phytoplankton growth
rate were tuned, separately for each coupled model, to reproduce the seasonal variability of N, and Chl in the near-surface of
North Pacific.

Compared to the InFlexPFT control, the FlexPFT model yields different growth rates because it instantaneously optimizes both

150   the allocation factor, f_V, and the Chl:C ratio of the chloroplast, $\hat{\theta}$, which appears in the light limitation term, $S(I,T)$ (Eq. 5).
Therefore, it is possible to understand the modeled patterns of phytoplankton biomass and production over the North Pacific by
comparing the expressions for growth rate, μ as a function of I, N, and T for each model, respectively. Results are presented
for simulated years 2000 to 2019. For the FlexPFT, the Chl concentration (mg m^{-3}) is the phytoplankton concentration, P
(mmol N m^{-3}), $\times \hat{\theta}/Q$, and Primary Production, PP (mgC m^{-3} day^{-1}), is $\mu_{Flex}P$ (Eq. 1) $\times$ the variable C:N ratio $(1/Q)$ (Eq.

155   2 and Smith et al., 2016). In the InFlexPFT, Chl concentration is $P \times$ the constant Chl:N ratio (1.59 g Chl (mol N)$^{-1}$), and PP
is $\mu_{InFlex}P$ (Eq. 7) $\times$ the fixed C:N ratio (Redfield ratio = 106:16 mol C (mol N)$^{-1}$).

2.3 Observational Data

Model results were compared with in-situ observations and satellite data (Chl, nitrate, and temperature). Sea surface Chl satel-
lite imagery is derived from the Moderate Resolution Imaging Spectroradiometer (MODIS) - Aqua (https://oceancolor.gsfc.nasa.gov),

160   using the seasonal climatological data of Level-3 global browser. Ship observed Chl data along the two sections (north-south
and east-west) in the North Pacific are available from the websites of the Japan Meteorological Agency, JMA (https://www.data.jma.go.jp),
and Japan Oceanographic Data Center, JODC (https://www.jodc.go.jp), respectively. Along the north-south section (165°E)
in the western North Pacific, JMA research vessels have observed regularly from 2005 to the present. Along the east-west
section (around 35°N) in the central North Pacific, observations were conducted from 2002 to 2003, summer, and pub-

165   lished by the JODC. Seasonal climatological nitrate and temperature distributions are acquired from the World Ocean At-

las 2018 (WOA18) (Garcia et al., 2018a; Locarnini et al., 2018). The PP data sets are available at three time-series stations: Stations K2 (47°N,160°E) and S1 (30°N,145°E) in the western North Pacific, as implemented by the K2S1 project (Matsumoto et al., 2014, 2016; Honda et al., 2017) (https://ebcrpa.jamstec.go.jp/k2s1/en/index.html), and Station ALOHA (22.45°N, 158°W) in the central North Pacific as operated under the Hawaii Ocean Time series (HOT) program (Karl et al.,
170   1996, 2021) (https://hahana.soest.hawaii.edu/hot/).

3   Results and Discussion

This section assesses the models' performance and examines the impact of physiological flexibility on modeled Chl and PP by comparing the results of two coupled physical-biological (FlexPFT and InFlexPFT) models against satellite imagery and vertical profiles of in-situ observations. The eddy-resolving ocean circulation model (OFES2) has fine horizontal resolution
175   (1/10°, about 10 km), and reproduces the western boundary current, Kuroshio, the observed variability in the Kuroshio Extension region between the subtropical and subpolar gyres, mesoscale eddies, and upwelling events (e.g., Masumoto et al., 2004; Sasai et al., 2010; Sasaki et al., 2020). These physical processes directly or indirectly affect the nutrient and light environments, and biogeochemical processes (e.g., Oschiles, 2002; Gruber et al., 2011; Levy et al., 2014; Sasai et al., 2010, 2019), and are important for supplying the nutrients needed by phytoplankton, especially in the coastal upwelling regions and the oligotrophic
180   subtropical gyre. Here we focus on the different assumptions about how phytoplankton growth rate depends on ambient nitrogen concentration and light intensity. First, the reproducibility of seasonal and horizontal Chl distributions is described. Next, we compare the results of the two coupled physical-biological models in terms of Chl and PP along two vertical transects (north-south and east-west, respectively) in the North Pacific, and discuss the reasons for the differences. Finally, the difference in PP as calculated by these two models over the North Pacific is also discussed.

185   ## 3.1   Surface Chl Pattern

The surface Chl distribution as simulated over the North Pacific by the two models is shown in Fig. 1, compared with MODIS-Aqua imagery to assess the two models' performance. Overall, the two models reproduce the climatological seasonal variations of surface Chl pattern between the subtropical and subpolar gyres, as captured by the MODIS-Aqua imagery. In addition, both models reproduce the boundary between the subtropical and subpolar gyres, its seasonal variations, and high concentration in
190   the coastal upwelling regions (California coast) as seen in the MODIS-Aqua imagery. Compared to the InFlexPFT, the FlexPFT model produces greater variations and steeper horizontal gradients of Chl concentration. Especially in the open ocean north of 30°N, coastal upwelling regions off the western coast of North America, the Sea of Okhotsk, and the Bering Sea, the FlexPFT produces higher surface Chl than the InFlexPFT, but underestimates Chl in the subtropical gyre (south of 30°N). The FlexPFT also reproduces greater seasonal variation of surface Chl in the subpolar gyre, similar to the pattern in the MODIS-Aqua
195   imagery. On the other hand, in the subtropical gyre, the InFlexPFT is more similar to the MODIS-Aqua imagery. These differences in the spatial and seasonal distributions of surface Chl result from the different phytoplankton growth rate equations, and especially the difference between the FlexPFT's variable Chl:C ratio (photoacclimation) versus the fixed ratio assumed in the

InFlexPFT.

3.2 Vertical Distributions of Chl and Primary Production

The limited data available from observations made by research vessels do capture key spatial and temporal distributions. As a characteristic vertical profile, the SCM varies seasonally and across ocean regions (Cullen, 1982), driven by different light attenuation levels and nutricline depths. It is impossible to capture the vertical profiles of Chl with satellite observations, and it is therefore important to verify the SCM field reproduced by the model using in-situ observations (e.g., Shulenberger and Reid, 1981; Furuya, 1990). Using a 3-D biogeochemical ocean model coupled with the same FlexPFT model, Masuda et al. (2021) showed that the observed global scale SCM distribution can be reproduced by incorporating photoacclimation in response to varying nutrient and light conditions. Here, the reproducibility of the vertical distribution of Chl for each model is discussed along two observation lines over the North Pacific: a north-south section along 165°E in Fig. 2, and an east-west section around 35°N in Fig. 3. In particular, we focus on the SCM formed in summer, and discuss the effects of different assumptions about how phytoplankton growth rate (Eqs. 1 and 7) depends on N concentration and light intensity, I, as well as their effects in combination with temperature, T (Figs. 4, 5, 6, and 7).

JMA research vessels have made observations on the north-south line along 165°E regularly since 1997, with good seasonal coverage. The best data coverage for vertical Chl profiles is available for the summer of 2006. The observed SCM (> 0.1 mg m^{-3}) depth varies from 50 m near the equator to 150 m in subtropical regions, and the FlexPFT clearly reproduces the observed pattern of SCM near the nutricline along the 165°E line (Fig. 2), with simulated values close to the observed SCM (Figs. 2a and 2c). However, the FlexPFT underestimates near-surface Chl. By contrast, the InFlexPFT (Fig. 2b) cannot reproduce the observed SCM even though its modeled distributions of N and T are similar to the corresponding observations (Figs. 2d, 2e, 2f, 2g, and 2h). The FlexPFT, which accounts for photoacclimation, reproduces the observed vertical Chl distributions much better than the InFlexPFT (Eqs. 1 and 7).

The vertical distribution of Chl also varies with longitude along the east-west transect around the boundary (35°N) between the subpolar and subtropical gyres (Fig. 3). The limited JODC Chl observations (Summer, 2001-2002) span the east and west of the North Pacific. The observed SCM (> 0.1 mg m^{-3}) appears between 50 and 150 m depth and deepens to the west (Fig. 3a), following the distribution of nutricline depths (Fig. 3d). Compared to the north-south transect, here the near-surface T gradient is not as steep (Figs. 2 and 3), with T increasing from the center to the east and west (Fig. 3g). The model reproduces the observed T distribution, and modeled N distribution is similar to the observed data (Figs. 3e, 3f, and 3h). The FlexPFT clearly reproduces the observed SCM around the nutricline depth (Figs. 3c and 3f) from east to west, whereas the InFlex does not (Fig. 3b). On the west side, both models overestimate the nutricline depth, and the FlexPFT underestimates the observed Chl (Figs. 3a and 3c) and N (Figs. 3d and 3f).

To clarify the mechanistic reasons for differences in the vertical distributions of Chl between the two models (Figs. 2 and 3), the vertical distributions of models' PP (mg C m^{-3}), and related phytoplankton growth rate (day^{-1}) from Eqs. 1 and 7, and the variable C:N ratio (reciprocal of the N quota of phytoplankton carbon ratio, $1/Q$) in the FlexPFT, are shown in Figs. 4 and 5.

235 The PP was calculated from the phytoplankton growth rate and the C:N ratio, which for the FlexPFT is variable (Figs. 4e and 5e) whereas it is constant for the InFlexPFT. Both models predict high PP near the surface in the subpolar regions along 165°E, with minimal PP near the bottom of the euphotic layer, which is close to 100 m depth (Figs. 4a and 4b). Overall, compared to the InFlexPFT, the FlexPFT produces greater PP, with profiles extending deeper into the subsurface (100 m depth) to the south of 30°N. Both models produce fast growth rates in the subpolar surface layers and the subtropical subsurface layers (Figs. 4c

240 and 4d). Especially in the subtropical subsurface layers, the FlexPFT predicts much faster growth than the InFlexPFT, and this difference in phytoplankton growth rate is reflected in the vertical distributions of Chl (Figs. 2b and 2c) and PP (Figs. 4a and 4b). The variable C:N ratio in the FlexPFT (Fig. 4e) also contributes substantially to its greater PP values (Fig. 4d), compared to the constant C:N ratio in the InFlexPFT (Fig. 4c). In Fig. 4e, the C:N ratio in the FlexPFT is high (> 20) near the surface around the equator and subtropical regions, and near the Redfield ratio (106:16 = 6.625) elsewhere in the subpolar region and

245 below the euphotic layer (below 100 m depth). Observed elemental ratios of phytoplankton and particulate organic matter in surface layers deviate substantially from the Redfield ratio (e.g., Garcia et al., 2018b; Liefer et al., 2019). Our results show that, compared to the assumption of constant C:N:Chl ratios, as in the InFlexPFT, accounting explicitly for variable C:N ratios and the acclimated growth response of phytoplankton, as in the FlexPFT, yields substantially better reproduction of Chl and PP profiles within the euphotic layer.

250

As in Fig. 4, the vertical distributions of modeled PP (mgC m^{-3}), related phytoplankton growth rate (day^{-1}) from Eqs. 1 and 7, and the variable C:N ratio in the FlexPFT in the east-west section are shown in Fig. 5. Both models predict high PP between 50 m and 100 m, with shallower distributions on the west side and deeper toward the east (Figs. 5a and 5b). Compared to the InFlexPFT, the FlexPFT predicts higher PP, especially in the subsurface (near 100 m depth). Although both models predict

255 faster growth on the west side, decreasing towards the east, their patterns differ (Figs. 5c and 5d). In the InFlexPFT, the phytoplankton growth rate is fastest near the surface and decreases with depth. On the other hand, the FlexPFT predicts increasing growth rate with depth from the surface to intermediate depths. Both models produce subsurface maxima in PP (Figs. 5a and 5b), with a stronger pattern for the FlexPFT model. The FlexPFT predicts an even stronger subsurface maximum in the vertical distribution of Chl (Fig. 3c). This results from the FlexPFT's combination of photoacclimation and variable C:N ratio, which is

260 consistently high (> 10) in the euphotic layer (0 - 100 m) (Fig. 5e). Below the euphotic layer and to the east side, the FlexPFT's C:N ratio approaches the Redfield ratio (106:16 = 6.625), and therefore the modeled Chl and PP differ less between the two models.

To examine the inter-dependent impacts of N concentration and light intensity, I on the phytoplankton growth rate in the

265 FlexPFT, as compared with their simple multiplicative dependencies in the InFlexPFT, Figs. 6 and 7 show scatter diagrams of modeled phytoplankton growth rate and variable C:N ratio ($1/Q$) versus N concentration (mmol N m^{-3}) at the three locations

along 165°E in Fig. 4 and around 35°N in Fig. 5. Compared to the InFlexPFT, the FlexPFT maintains faster growth as either light or nutrient becomes limiting everywhere. The phytoplankton growth rate also depends on temperature, T (Eqs. 1 and 7), as shown by colors. In general, I and T both depend on latitude, and both decrease with increasing depth. At 25°N latitude

270   (Figs. 6a and 6d), in the subtropical gyre, both models predict phytoplankton growth rates exceeding 0.2 (day^{-1}) near the surface, despite the low N concentrations (< 0.1 mmol N m^{-3}). Compared to the InFlexPFT, the FlexPFT maintains faster growth rates at the surface and 50 m because it dynamically allocates intracellular resources to cope with variations in N concentration and I (Smith et al., 2016, and Eq. 1). At the boundary between the subtropical and subpolar gyres, which lies approximately between 35°N and 40°N latitude, the two models predict clearly different patterns of phytoplankton growth rate

275   compared to those at 25°N (Figs. 6b, 6c, 6e, and 6f). At the gyre boundary and in the subarctic, both models tend to produce faster growth rates at 50 m, where the availability of light and nutrients is better balanced to support phytoplankton growth, compared to the surface and 100 m depth. Compared to temperature, nutrient- and light-limitation exert greater control over the modeled growth rates with both models, but more so for the FlexPFT. Nutrient limitation is the strongest determinant of growth rates at the surface and intermediate (50 m) depth, whereas light limitation strongly suppresses growth rates (and their

280   range of variability) at 100 m depth.

Similar to Fig. 6, Fig. 7 shows modeled phytoplankton growth rates at three selected locations along the 35°N latitude transect (Fig. 5). The two locations (160°E, 36°N, and 170°E, 34°N) on the west side of the North Pacific are close to (165°E, 35°N) in Fig. 6, and have similar characteristics. At these locations, near the boundary of the subtropical and subpolar gyres, the

285   nutricline depth is shallower than on the eastern side. The InFlexPFT at the surface and 50 m depth shows the two curves of phytoplankton growth rate depending on the N concentration, I, and T (Figs. 7a and 7b) similar to Fig. 6b. Again, the InFlexPFT predicts the fastest growth rates at the highest T, despite low N concentrations. On the other hand, the FlexPFT's growth rates are more clearly related to ambient N concentration with a less apparent relationship to T, despite assuming the same T dependence in both models (Figs. 7d and 7e). As in Fig. 6, compared to the InFlexPFT, the FlexPFT predicts

290   faster phytoplankton growth rates, with maximal growth at intermediate N concentrations (despite lower T compared to the surface), and wider variation of growth rate. At the eastern-most location (170°W, 30°N) shown in the right-most column of Figs. 7c and 7f, the patterns are more similar to the subtropical area shown in the left-most column of Figs. 6a and 6d, albeit with somewhat greater variability of growth rate for both models near the surface, where temperatures are high and nutrients scarce. As at the subtropical location (25°N latitude) shown in the left-most column of Fig. 6, at this location the InFlexPFT

295   also exhibits a stronger apparent temperature sensitivity (hence a wider range of growth rates) than the FlexPFT, but here only near the surface. Neither model shows a strong apparent relationship between growth rate and N concentration at this location, indicating which seems to indicate that light, nutrients, and temperature all substantially limit the growth here.

Compared to the InFlexPFT, the FlexPFT produces higher PP because its variable C:N ratio substantially exceeds the Redfield

300   ratio (106:16 = 6.625), with a consistent increase in C:N ratio from intermediate depths to the surface everywhere (Figs. 6 and 7). Where the phytoplankton growth rate reaches maximal values at 35°N and 40°N, the C:N ratios are between 10 and 15

(Figs. 6h, 6i, 7g, and 7h), which enhances PP (Figs. 4b and 5b). Along the east-west transect as well (Fig. 7), the FlexPFT again predicts maximal C:N ratios near the surface, where nutrient concentrations are lowest and light (and temperature) levels are highest, with a similar range of C:N ratios as along the north-south transect (Fig. 6). On the west side, the C:N ratio in the FlexPFT (Figs. 7g and 7h) exceeds the Redfield ratio, except below the euphotic layer, and growth rates are maximal at intermediate nutrient concentrations and light intensities. On the other hand, on the east side, where ambient nutrient concentrations are consistently low, despite the high C:N ratio in the FlexPFT (Fig. 7i), modeled growth rates differ little between the two models.

Overall, at the surface and 50 m depth, the modeled patterns of growth rate versus N concentration are more clearly separated with the FlexPFT model, which produces a steeper and more consistent increase in growth rate from low to intermediate N concentrations, compared to the InFlexPFT. These variations in the locally realized maximum growth rate result from the FlexPFT's growth optimization scheme, which re-allocates intracellular resources, resulting in an inter-dependent response to I and N availability (Fig. 3 of Smith et al., 2016, and Eq. 1). By contrast, the InFlexPFT's simple multiplicative dependencies on I and N concentration result in a steeper decrease in growth rate as either resource becomes limiting. Despite the assumption of the same inherent T sensitivity for both models, the optimal resource allocation thus results in a weaker apparent relationship between modeled growth rates and ambient T in the FlexPFT model, which predicts the fastest growth rates at intermediate N concentrations despite lower T than at the surface. By contrast, the InFlexPFT model, because of its weaker dependence on nutrient concentration and light, predicts the fastest growth rates at the highest temperatures, with a stronger apparent relationship between growth rate and ambient temperature.

3.3 Primary Production

The vertical distribution of PP differs along the two transect lines (north-south and east-west, respectively) (Figs. 4 and 5). To investigate the models' PP variations within the euphotic layer, Fig. 8 shows the seasonal variations of vertically integrated PP from the surface to 100 m depth for the two models. The InFlexPFT produces weak seasonality for PP (Figs. 8a, 8b, 8c, and 8d), with maximal values in spring (> 800 mg C m^{-2} day^{-1}) at the boundary between the subtropical and subpolar gyres (Fig.8b), because the spring bloom occurs both horizontally and vertically (e.g., Fig. 1f). Along the east-west transect, from 30°N to 40°N, PP varies with N concentration, which is high on the west side and low on the east side (Figs. 3d, 3e, and 3f). In summer and fall, when N concentration in the subtropical gyre decreases in the euphotic layer, even where light intensity, I, is sufficient, N availability limits the phytoplankton growth rate (Eq. 7), so that PP does not increase (Figs. 8c and 8d). On the other hand, in the subpolar gyre, the PP in winter, summer, and fall increase with N (Fig. 8a). In the coastal upwelling regions, N supplied from below the euphotic layer sustains higher PP compared to the open ocean. The FlexPFT predicts wider seasonal variations of PP across the North Pacific (Figs. 8e, 8f, 8g, and 8h), which are especially noticeable at the boundary between the subtropical and subpolar gyres, along the Kuroshio Current flowing south of Japan, and in the coastal upwelling region off California. The FlexPFT's springtime PP reaches twice (> 1600 mg C m^{-2} day^{-1}) that of the InFlexPFT (Figs. 8b

and 8f). In the subtropical gyre, where the light intensity in the euphotic layer is sufficient for phytoplankton growth (Eq. 1), N concentration in winter is higher than in summer and fall, and as a result, PP values are relatively high, although still lower than during spring (Fig. 8e). In the subpolar gyre, where N concentrations are high, as the light environment improves from winter to summer, PP increases within the euphotic layer (Figs. 8g and 8h). In the coastal upwelling regions and the Kuroshio

340   Extension, the FlexPFT, because of its optimal resource allocation, predicts much greater PP than the InFlexPFT. These spatial and seasonal differences in modeled patterns result from the different underlying assumptions about how phytoplankton respond to changing conditions. As found in previous studies (Anugerahanti et al., 2021; Kerimoglu et al., 2021; Masuda et al., 2021), our results show that photoacclimation and variable C:N:Chl ratios, as represented by the FlexPFT, are important for capturing observed distributions of PP and especially the SCM. For reproducing the latter, capturing the unimodal distribution

345   of Chl;C ratio over depth is particularly important (Chen and Smith, 2018; Kerimoglu et al., 2021).

Fig. 9 shows a direct comparison of modeled and observed vertical profiles of PP, for three time-series stations in the North Pacific: Station K2 in the western subpolar gyre, and Stations S1 and ALOHA in the western and eastern subtropical gyre, respectively. At Station K2, the temporal variation of observed PP is most significant above 25 m depth, and less variable

350   below 25 m depth (Fig. 9a). Overall, compared to the FlexPFT, the InFlexPFT predicts less temporal variability of PP, except below 50 m depth at Station K2, where the InFlexPFT predicts faster growth than the FlexPFT (Figs. 4c and 4d). At Station S1, the temporal variation of observed PP is greater above 50 m depth, with less variability below 50 m depth (Fig. 9b). Compared to the subpolar gyre, in the subtropical gyre the highest PP occurs deeper, where light limitation is more substantial, which suggests that PP could be enhanced by an increase in light levels despite the relatively low N concentrations. Compared to

355   the InFlexPFT, the FlexPFT shows greater temporal variation of PP above 75 m depth. This difference depends on whether the phytoplankton growth ratio calculated by the model can reflect the optimal N and light environment (using FlexPFT or InFlexPFT). Unlike the two stations in the western North Pacific, at Station ALOHA, both models underestimate the observed PP (Fig. 9c). The observed PP from the surface to 100 m depth is large, and PP near the surface is about the same as at the western Station S1. The FlexPFT underestimates the mean PP, but the temporal variation is closer to the observed variability

360   than with the InFlexPFT. Overall, compared to the InFlexPFT, the FlexPFT agrees better with the observed PP profiles.

The difference in phytoplankton growth rate between the two models is reflected in the spatiotemporal distribution of PP (Figs. 8, and 9), similar to Chl distribution (Figs. 1, 2, and 3). These differences are greatest in the boundary region between the subporal and subtropical gyres, the subpolar gyre, and the coastal upwelling region. Also, the FlexPFT reproduces greater temporal

365   variations than the InFlexPFT, which is more consistent with the observed variability. These results indicate that the FlexPFT (which incorporates photoacclimation and variable C:N:Chl ratios) better captures seasonal changes within the euphotic layer and near the nutricline than the InFlexPFT. Estimated primary production in the North Pacific basin (20°N - 60°N, 130°E - 110°W) from Fig. 8 with the FlexPFT is 5.0 - 5.6 PgC yr^{-1}, and with the InFlexPFT is 2.3 - 2.5 PgC yr^{-1} over the simulated period of 2000 - 2019, respectively, and the FlexPFT's estimate is about twice that of the InFlexPFT. On the other hand, the

370   global primary production as estimated by the satellite data and global biogeochemical models ranges widely: from 38.8 - 42.1

PgC yr^{-1} over the period of 1998 - 2018 (Kulk et al., 2020) and from 38 - 79 PgC yr^{-1} (Carr et al., 2006). The FlexPFT's modeled PP for the North Pacific basin amounts to approximately 10% of the estimated global primary production.

4   Conclusions

375   We have investigated the adaptive response of phytoplankton growth to changing light, nutrient, and temperature conditions over the North Pacific using two physical-biological models. We compared modeled phytoplankton biomass and primary production from a recently developed phytoplankton model, FlexPFT (Smith et al., 2016), which incorporates photoacclimation and variable C:N:Chl ratios for changing light and nutrient conditions, and the InFlexPFT control, which lacks photoacclimation and assumes constant C:N:Chl ratios (fixed stoichiometry). Both models reproduce broad features of the climatological

380   seasonal variations of surface Chl across the North Pacific, as captured by MODIS-Aqua imagery (Fig.1). In terms of contrast between the subtropical and subpolar gyres, compared to the InFlexPFT, the FlexPFT produces greater variations in modeled surface Chl. Vertical profiles of modeled Chl also differ between the two models, with the FlexPFT reproducing better the observed SCM near the nutricline depth along 165°E (north-south section, Fig. 2) and around 35°N (east-west section, Fig. 3). In contrast to the FlexPFT, the InFlexPFT cannot reproduce the observed SCM even though the N distributions in the two

385   models are similar. Compared to the InFlexPFT, the inclusion of photoacclimation and variable C:N:Chl ratios in the FlexPFT yields a more apparent separation of the limiting effects of light, nutrients, and temperature, which reproduces substantially better the observed Chl and PP distributions.

In both models, phytoplankton growth rate depends on the light intensity, nutrient concentration, and temperature (Eqs. 1 and

390   7 in Section 2.2), but the different functional forms of the light and nutrient dependencies in the two models produce substantially different distributions of Chl and PP. In the FlexPFT, the optimization of phytoplankton growth rate subject to the trade-off between light and nutrient acquisition yields an inter-dependent response to light and nutrient limitation. Compared to the typical assumption of straightforward multiplicative effects of light and temperature, as in the InFlexPFT control, this interdependent response allows more efficient growth as either light or nutrient becomes limiting. The FlexPFT also produces

395   greater C:N ratios than the InFlexPFT, especially near the surface (Figs. 4, 5, 6, and 7), and different horizontal and vertical Chl distributions, especially, in the boundary region between subtropical and subpolar gyres (Figs. 2, and 3). In the oligotrophic subtropical gyre, the FlexPFT predicts slow growth near the surface where N concentration is very low, but its Chl concentration is higher than that of InFlexPFT near the nutricline depth. Compared to the InFlexPFT, the FlexPFT predicts faster growth even at low N concentration (< 0.1 mmol N m^{-3}), and enhanced Chl concentration from the surface to intermediate

400   depths. In the boundary region, both light intensity and N concentration limit the growth rate. Compared to the InFlexPFT, the FlexPFT predicts maximal growth in the subsurface layer, rather than near the surface, and its variable Chl:C ratio allows better reproduction of the observed SCM. In the subpolar gyre, the surface layer provides the optimum environment (light intensity and N concentration) for phytoplankton growth in both models, but the FlexPFT produces higher Chl concentrations because

of its variable Chl:C ratio (Figs. 4, 5, 6, and 7).

405

Our comparison of model results against summertime observations from the North Pacific revealed that, compared to the in-flexible control model, the incorporation of photoacclimation and variable C:N:Chl ratios for changing light, nutrient, and temperature conditions in the FlexPFT yields improved reproduction of observed Chl and primary production distributions in the near-surface ocean. The IA assumption allowed computationally efficient modeling of flexible phytoplankton composition

410 and growth response in our regional model, which should be of even greater value for global-scale biogeochemical models. In the future we plan to assess model performance for other seasons and years, and to apply this approach in a global ocean biogeochemical model in order to examine the response of phytoplankton biomass and primary production to climate change.

Data availability. The OFES2 coupled NPZD model simulations are available upon request. Observed data used in this study are available at

415 the following sites: The surface Chl satellite imagery of MODIS-Aqua data is available for download at https://oceancolor.gsfc.nasa.gov. The vertical observed Chl data are available for download at Japan Meteorological Agency (https://www.data.jma.go.jp) and Japan Oceanographic Data Center (https://www.jodc.go.jp). WOA09 and WOA18 are available at https://www.ncei.noaa.gov (Antonov et al., 2010; Garcia et al., 2010; Locarnini et al., 2010; Garcia et al., 2018a; Locarnini et al., 2018). The primary production data sets at Stations K2 and S1, and Station ALOHA are available for download at https://ebcrpa.jamstec.go.jp/k2s1/en/index.html (Matsumoto et al., 2014, 2016; Honda et al., 2017)

420 and https://hahana.soest.hawaii.edu/hot/ (Karl et al., 1996, 2021), respectively.

Appendix A: NPZD model

The NPZD model in the OFES2 is defined as nitrogen, N, phytoplankton, P, zooplankton, Z, and detritus, D, based on Sasai et al. (2006, 2010, 2016). The evolution of biological tracer concentration, B_i, is governed by an advective-diffusive-reactive equation.

425
$$\frac{\partial B_i}{\partial t} = -\nabla \cdot (uB_i) + \nabla \cdot (k\nabla B_i) + sms(B_i) \tag{A1}$$

where u is velocity vector of OFES2, k is the lateral and vertical diffusion coefficients in the OFES2, and $sms(B_i)$ is the source-minus-sink (sms) term due to biological activity rate (mmol N m^{-3} day^{-1}) in the NPZD model. For the individual tracers (P, Z, D and N), the sms terms are given by:

$$sms(P) = \mu P - r_P P - \delta_P P^2 - \lambda \mu P - G(P)Z \tag{A2}$$

430
$$sms(Z) = G(P)Z - (\gamma_1 - \gamma_2)G(P)Z - (1 - \gamma_1)G(P)Z - \delta_Z Z^2 \tag{A3}$$

$$sms(D) = \delta_P P^2 + (1 - \gamma_1)G(P)Z + \delta_Z Z^2 - \delta_D D - \frac{\partial}{\partial z}(W_s D) \tag{A4}$$

$$sms(N) = -\mu P + r_P P + \lambda \mu P + (\gamma_1 - \gamma_2)G(P)Z + \delta_D D \tag{A5}$$

where the five terms of the right-hand side in the $sms(P)$ are the phytoplankton growth, μ, the respiration of P (r_P, 0.12 day^{-1}, is the respiration rate for P), the mortality of P (δ_P, 0.24 day^{-1}, is the mortality rate for P), the extracellular excretion

435   of P (λ, 0.135 (no dim.), is the extracellular excretion rate of P), and the grazing of P by Z ($G(P)$ is the grazing rate equation of Sasai et al., 2016). In this study, we adopt two different formulations of phytoplankton growth (FlexPFT and InFlexPFT, see Section 2.2), μ, to the first term of the right-hand side in the $sms(P)$ in Eq. A2. The four terms of $sms(Z)$ are the grazing of P by Z, the excretion of Z (γ_1, 0.7 (no dim.), is the assimilation efficiency of Z, and γ_2, 0.3 (no dim.), is the growth efficiency of Z), the egestion of Z, and the mortality of Z (δ_Z, 0.12 day^{-1}, is the mortality rate for Z). The six terms of $sms(D)$ are the

440   mortality of P, the egestion of Z, the mortality of Z , the decomposition from D to N (δ_D, 0.3 day^{-1}, is the decomposition rate from D to N) and the sinking of D (W_s, 30 m day^{-1} upper 1000 m or 300 m day^{-1} below 1000 m, is sinking velocity). The five terms of $sms(N)$ are the phytoplankton growth, the respiration of P, the extracellular excretion of P, the excretion of Z, and the decomposition from D to N. More details of biological parameters are described by Sasai et al. (2006, 2010, 2016).

Author contributions. YS, SLS, HS and MN designed the study and YS simulated two biological models. SLS also developed the FlexPFT

445   model. ES prepared the satellite and observation data for comparison with the model results. All authors contributed significantly to the writing of the paper.

Competing interests. The authors declare that they have no conflict of interest.

Acknowledgements. OFES2 simulations were conducted on the Earth Simulator under the support of the Japan Agency for Marine-Earth Science and Technology (JAMSTEC).

450   *Financial support.* This research has been supported by the Japan Society for the Promotion of Science (JSPS) KAKENHI Grand Numbers, JP17K05663, JP19H05701, JP20K04075, and JRPs-LEAD with DFG.

References

Anderson, T. R.: Progress in marine ecosystem modelling and the "unreasonable effectiveness of mathematics", J. Mar. Syst., 81, 4-11, https://doi.org/10.1016/j.jmarsys.2009.12.015, 2010.

455 Antonov, J. I., Seidov, D., Boyer, T. P., Locarnini, R. A., Mishonov, A. V., Garcia, H. E., Baranova, O. K., Zweng, M. M., and Johnson, D. R.: World Ocean Atlas 2009, Volume 2: Salinity. S. Levitus, Ed. NOAA Atlas NESDIS 69, U.S. Government Printing Office, Washington, D.C., 184 pp., 2010.

Anugerahanti, P., Kerimoglu, O., and Smith, S. L.: Enhancing ocean biogeochemical models with phytoplankton variable composition, Front. Mar. Sci., 8:675428, https://doi:10.3389/fmars.2021.675428, 2021.

460 Ayata, S.-D., Lévy, M., Aumont, O., Sciandra, A., Sainte-Marie, J., Tagliabue, A., and Bernard, O.: Phytoplankton growth formulation in marine ecosystem models: Should we take into account photo-acclimation and variable stoichiometry in oligotrophic areas?, J. Mar. Syst., 125, 29-40, https://dx.doi.org/10.1016/j.jmatsys.2012.12.010, 2013.

Baklouti, M., Diaz, F., Pinazo, C., Faure, V., and Quéguiner, B.: Investigation of mechanistic formulations depicting phytoplankton dynamics for models of marine pelagic ecosystems and description of a new model, Prog. Oceanogr., 71, 1-33,
465 https://doi.org/10.1016/j.pocean.2006.05.002, 2006.

Caperon, J.: Population growth response of Isochrysis galbana to nitrate variation at limiting concentrations, Ecology, 49, 866-872, https://doi.org/10.2307/1936538, 1968.

Carr, M.-E., Friedrichs, M. A. M., Schmeiz, M., Aita, M. N., Antoine, D., Arrigo, K. R., Asanuma, I., Aumont, O., Barber, R., Behrenfeld, M., Bidigare, R., Buitenhuis, E. T., Campbell, J., Ciotti, A., Dierssen, H., Dowell, M., Dunne, J., Esaias, W., Gentili, B., Gregg, W.,
470 Groom, S., Hoepffner, N., Ishizaka, J., Kameda, T., Quéré, C. L., Lohrenz, S., Marra, J., Mélin F., Moore, K., Morel, A., Reddy, T. E., Ryan, J., Scardi, M., Smyth, T., Turpie, K., Tilstone, G., Waters, K., and Yamanaka, Y.: A comparison of global estimates of marine primary production from ocean color, Deep-Sea Res., Part II, 53, 741-770, https://doi.org/10.1016/j.dsr2.2006.01.028, 2006.

Chen, B., and Smith, S. L.: Optimality-based approach for computationally efficient modeling of phytoplankton growth, chlorophyll-to-carbon, and nitrogen-to-carbon ratios, Ecological Modelling, 385, 197-212, https://doi.org/10.1016/j.ecolmodel.2018.08.001, 2018.

475 Cullen, J. J.: The deep chlorophyll maximum: Comparing vertical profiles of chlorophyll a, Can. J. Fish. aquat. Sciences, 39, 791-803, https://doi.org/10.1139/f82-108, 1982.

Droop, M. R.: Vitamin B12 and marine ecology, IV. The kinetics of uptake, growth and inhibition in Monochrysis lutheri, J. Mar. Biol. Assoc. U.K., 48, 689-733, https://doi.org/10.1017/S0025315400019238, 1968.

Droop, M. R.: 25 years of algal growth kinetics, Bot. Mar., 26, 99-112 , https://doi.org/10.1515/botm.1983.26.3.99, 1983.

480 Edwards, K. F., Thomas, M. K., Klausmeier, C. A., and Litchman, E.: Allometric scaling and taxonomic variation in nutrient utilization traits and maximum growth rate of phytoplankton, Limnol. Oceaonogr, 57, 554-566, https://doi.org/10.4319/lo.2012.57.2.0554, 2012.

Falkowski P. G., Dubinsky, Z., and Wyman, K.: Growth-irradiance relationships in phytoplankton, Limnol. Oceanogr., 30, 311-332, https://doi.org/10.4319/lo.1985.30.2.0311, 1985.

Field, C. B., Behrenfeld, M. J., Randerson, J. T., and Falkowski, P.: Primary production of the biosphere: integrating terrestrial and oceanic
485 components. Science, 281, 237-240.

Flynn, K. J.: Do we need complex mechanistic photoacclimation models for phytoplankton?, Limnol. Oceanogr., 48, 2243-2249, https://doi.org/10.4319/lo.2003.48.6.2243, 2003.

Flynn, K. J.: Ecological modelling in a sea of variable stoichiometry: Dysfunctionality and the legacy of Redfield and Monod, Prog. Oceanogr., 84, 52-65, https://doi.org/10.1016/j.pocean.2009.09.006, 2010.

490 Franks, P. J. S.: Planktonic ecosystem models: Perplexing parameterizations and a failure to fail, J. Plankton Res., 31, 1299-1306, https://doi.org/10.1093/plankt/fbp069, 2009.

Follows, M. J., Dutkiewicz, S., Grant, S., and Chisholm, S. W.: Emergent biogeography of microbial communities in a model ocean, Science, 315, 1843-1846, https://doi.org/10.1126/science.1138544, 2007.

Furuya, K.: Subsurface chlorophyll maximum in the tropical and subtropical western Pacific Ocean: Vertical profiles of phy-
495 toplankton biomass and its relationship with chlorophyll a and particulate organic carbon, Mar. Biol., 107, 529-539, https://doi.org/10.1007/BF01313438, 1990.

Garcia, H. E., Locarnini, R. A., Boyer, T. P., Antonov, J. I., Zweng, M. M., Baranova, O. K., and D. R. Johnson, D. R.: World Ocean Atlas 2009, Volume 4: Nutrients (phosphate, nitrate, silicate). S. Levitus, Ed. NOAA Atlas NESDIS 71, U.S. Government Printing Office, Washington, D.C., 398 pp., 2010.

500 Garcia, H. E., Weathers, K., Paver, C. R., Smolyar, I., Boyer, T. P., Locarnini, R. A., Zweng, M. M., Mishonov, A. V., Baranova, O. K., Seidov, D., and Reagan, J. R.: World Ocean Atlas 2018, Volume 4: Dissolved Inorganic Nutrients (phosphate, nitrate and nitrate+nitrite, silicate). A. Mishonov Technical Ed.; NOAA Atlas NESDIS 84, 35pp., 2018a.

Garcia, N. S., Sexton, J., Riggins, T., Brown, J., Lomas, M. W., and Martiny, A. C.: High variability in cellular stoichiometry of carbon, nitrogen, and phosphorus within classes of marine eukaryotic phytoplankton under sufficient nutrient conditions, Front. Microbiol., 9:543,
505 https://doi.org/10.3389/fmicb.2018.00543, 2018b.

Geider, R. J., Maclntyre, H. L., and Kana, T. M.: A dynamic regulatory model of phytoplanktonic acclimation to light, nutrients, and temperature, Limnol. Oceanogr., 43, 679-694, https://doi.org/10.4319/lo.1998.43.4.0679, 1998.

Goldman, J. C., McCarthy, J. J., and Peavey, D. G.: Growth rate influence on the chemical composition of phytoplankton in oceanic waters, Nature, 279, 210-215, 1979.

510 Gruber, N., Lachkar, Z., Frenzei, H., Marchesiello, P., Münnich, M., McWilliams, J. C., Nagai, T., and Plattner, G-K.: Eddy-induced reduction of biological production in eastern boundary upwelling systems, Nature Geosci., 4, 787-792, https://doi.org/10.1038/ngeo1273, 2011.

Honda, M. C., Wakita, M., Matsumoto, K., Fujiki, T., Siswanto, E., Sasaoka, K., Kawakami, H., Mino, Y., Sukigara, C., Kitamura, M., Sasai, Y., Smith, S. L., Hashioka, T., Yoshikawa, C., Kimoto, K., Watanabe, S., Kobari, T., Nagata, T., Hamasaki, K., Kaneko, R., Uchimiya, M., Fukuda, H., Abe, O., and Saino, T.: Comparison of carbon cycle between the western Pacific subarctic and subtropical time-series
515 stations: highlights of the K2S1 project. J. Oceanogr., 73, 647-667, https://doi.org/10.1007/s10872-017-0423-3, 2017.

Karl, D. M., Christian, J. R., Dore, J. E., Hebel, D. V., Letelier, R. M., Tupas, L. M., and Winn, C. D.: Seasonal and interannual variability in primary production and particle flux at Station ALOHA, Deep-Sea Res. II, 43, 539-568, https://doi.org/10.1016/0967-0645(96)00002-1, 1996.

Karl, D. M., Letelier, R. M., Bidigare, R. R., Björkman, K. M., Church, M. J., Dore, J. E., and White, A. E.: Seasonal-
520 to-decadal scale variability in primary production and particulate matter export at Station ALOHA, Prog. Oceanogr., 195, https://doi.org/10.1016/j.pocean.2021.102563, 2021.

Kerimoglu, O., Anugerahanti, P., and Smith, S. L.: FABM-NflexPD 1.0: assessing an instantaneous acclimation approach for modeling phytoplankton grwoth, Geosci. Model Dev., 14, 6025-6041, https://doi.org/10.5194/gmd-14-6025-2021, 2021.

Komori, N., Takahashi, K., Komine, K., Motoi, T., Zhang, X., and Sagawa, G.: Description of sea-ice compartment of coupled ocean-sea-ice
525 model for the Earth Simulator (OIFES), J. Earth Simulator, 4, 31-45, 2005.

Kulk, G., Platte, T., Dingle, J., Jackson, T., Jönsson, B. F., Bouman, H. A., Babin, M., Brewin, R. J. W., Doblin, M., Estrada, M., Figueiras, F. G., Furuya, K., González-Benítez, N., Gudfinnsson, H. G., Gudmundsson, K., Huang, B., Isada, T., Kovač, Ž., Lutz, V. A., Marañón, E., Raman, M., Richardson, K., Rozema, F. D., van de Poll, W. H., Segura, V., Tilstone, G. H., Uitz, J., van Dongen-Vogels, V., Yoshikawa, T., and Sathyendranath, S.: Primary production, an index of climate change in the ocean: Satellite-based estimatets over two decades, Remote Sens., 12, 826, https://doi.org/10.3390/rsl2050826, 2020.

Levy, M., Resplandy, L., and Lengaigne, M.: Oceanic mesoscale turbulence drives large biogeochemical interannual variability at middle and high latitude, Geophys. Res. Lett., https://doi.org/10.1002/2014GL059608, 2014.

Liefer, J. D., Garg, A., Fyfe, M. H., Irwin, A. J., Benner, I., Brown, C. M., Follows, M. J., Omta, A. W., and Finkel, Z. V.: The macromolecular basis of phytoplankton C:N:P under nitrogen starvation, Front. Microbial., 10:763, https://doi.org/10.3389/fmicb.2019.00763, 2019.

Locarnini, R. A., Mishonov, A. V., Antonov, J. I., Boyer, T. P., Garcia, H. E., Baranova, O. K., Zweng, M. M., and Johnson, D. R.: World Ocean Atlas 2009, Volume 1: Temperature. S. Levitus, Ed. NOAA Atlas NESDIS 68, U.S. Government Printing Office, Washington, D.C., 184 pp., 2010.

Locarnini, R. A., Mishonov, A. V., Baranova, O. K., Boyer, T. P., Zweng, M. M., Garcia, H. E., Reagan, J. R., Seidov, D., Weathers, K., Paver, C. R., and I. Smolyar, I.: World Ocean Atlas 2018, Volume 1: Temperature. A. Mishonov Technical Ed.; NOAA Atlas NESDIS 81, 52pp., 2018.

Martiny, A. C., Pham, C. T. A., Primeau, F. W., Vrugt, J. A., Moore, J. K., Levin, S. A., and Lomas, M. W.: Strong latitudinal patterns in the elemental ratios of marine plankton and organic matter, Nature Geosciences, 6, 279-283, https://doi.org/10.1038/ngeo1757, 2013.

Masuda, Y., Yamaka, Y., Smith, S. L., Hirata, T., Nakano, H., Oka, A., and Sumata, H.: Photoacclimation by phytoplankton determines the distribution of global subsurface chlorophyll maxima in the ocean, communications earth & environment, 2:128, https:/doi.org/10.1038/s43247-021-00201-y, 2021.

Masumoto, Y., Sasaki, H., Kagimoto, T., Komori, K., Ishida, A., Sasai, Y., Miyama, T., Motoi, T., Mitsudera, H., Takahashi, K., Sakuma, H., and Yamagata, T.: A fifty-year eddy-resolving simulation of the world ocean -Preliminary outcomes of OFES (OGCM for the Earth Simulator)-, J.Earth Simulation, 1, 35-56, 2004.

Matsumoto, K., Honda, M. C., Sasaoka, K., Wakita, M., Kawakami, H., and Watanabe, S.: Seasonal variability of primary production and phytoplankton biomass in the western Pacific subarctic gyre: Control by light availability within the mixed layer, J. Geophys. Res. Oceans, 119, 6523-6354, https://doi.org/10.1002/2014JC009982, 2014.

Matsumoto, K., Abe, O., Fujiki, T., Sukigara, C., and Mino, Y.: Primary productivity at the time-series stations in the northwestern Pacific Ocean: is the subtropical station unproductive?, J. Oceanogr., 72, 359-371, https://doi.org/10.1007/s10872-016-0354-4, 2016.

Monod, J.: The growth of bacterial cultures, Annu. Rev. Microbiol., 3, 371-394, 1949.

Moore, J. K., Doney, S. C., Kleypes, J. A., Glover, D. M., and Fung, I. Y.: An intermediate complexity marine ecosystem model for the global domain, Deep-Sea Res. II, 49, 403-462, https://doi.org/10.1016/50967-0645(01)00108-4, 2001.

Oschlies, A.: Can eddies make ocean deserts bloom? Global Biogeochem. Cycles, 16, 1106, https://doi.org/10.1029/2001GB001830, 2002.

Platt, T., and Jassby, A. D.: The relationship between photosynthesis and light for natural assemblages of coastal marine phytoplankton, J. Phycol., 12, 421-430, https://doi.org/10.1111/j.1529-8817.1976.tb02866x, 1976.

Pahlow, M.: Linking chlorophyll-nutrient dynamics to the Redfield N:C ratio with a model of optimal phytoplankton growth, Mar. Ecol. Prog. Ser., 287, 33-43, https://doi.org/10.3354/meps287033, 2005.

Pahlow, M., Dietz, H., and Oschlies, A.: Optimal-based model of phytoplankton growth and diazotrophy, Mar. Ecol. Prog. Ser., 489, 1-16, https://doi.org/10.3354/meps10449, 2013.

Pahlow, M., and Oschlies, A.: Optimal allocation backs Droop's cell-quota model, Mar. Ecol. Prog. Ser., 473, 1-5,
565   https://doi.org/10.3354/meps10181, 2013.

Redfield, A. C., Ketchum, B. H., and Richards, F. A.: The influence organisms on the composition of sea water, In: Hill, H. M. (Ed.), The
       Sea, Wiley, New York, PP,26-77, 1963.

Sasai,Y., Ishida, A., Sasaki, H., Kawahara, S., Uehara, H., and Yamanaka, Y.: A global eddy-resolving coupled physical-biological model:
       Physical influences on a marine ecosystem in the North Pacific, Simulation, 82, .467-474, 2006.

570   Sasai, Y., Richards, K. J., Ishida, A., and Sasaki, H.: Effects of cyclonic eddies on the marine ecosystem in the Kuroshio Extension region
       using an eddy-resolving coupled physical-biological model, Ocean Dynamics, 60(3), 693-704, https://doi.org/10.1007/s10236-010-0264-
       8, 2010.

Sasai, Y., Yoshikawa, C., Smith, S. L., Hashioka, T., Matsumoto, K., Wakita, M., Sasaoka, K., and Honda, M. C.: Coupled 1-D physical-
       biological model study of phytoplankton production at two contrasting time-series stations in the western North Pacific, J.Ocenogr., 72,
575   509-526, https://doi.org/10.1007/s10872-015-0341-1, 2016.

Sasai, Y., Honda, M. C., Siswanto, E., Kato, S., Uehara, K., Sasaki, H., and Nonaka, M.: Impact of ocean physics on marine ecosystems in
       the Kuroshio and Kuroshio Extension regions: A high-resolution coupled physical-biological model study. In: Kuroshio Current: Physical,
       Biogeochemical and Ecosystem Dynamics, Takeyoshi Nagai, Hiroaki Saito, Koji Suzuki, Motomitsu Takahashi (eds.), AGU Geophysical
       Monograph Series. AGU-Wiley, pp 175-188, 10 April 2019, https://doi.org/10.1002/9781119428428.ch11, 2019.

580   Sasaki, H., Kida, S., Furue, R., Aiki, H., Komori, N., Masumoto, Y., Miyama, T., Nonaka, M., Sasai, Y., and Taguchi, B.: A global eddying
       hindcast ocean simulation with OFES2, Geoscientific Model Development, 13, 3319-3336, https://doi.org/10.5194/gmd-13-3319-2020,
       2020.

Shulenberger, E., and Reid, J. L.: The Pacific shallow oxygen maximum, deep chlorophyll maximum, and primary productivity, reconsidered,
       Deep-Sea Res., 28, 901-919, https://doi.org/10.1016/0198-0149(81)90009-1, 1981.

585   Smith, G. J., Ziimmerman, R. C., and Alberte, R. S.: Molecular and physiological responses of diatoms to variable levels of irradi-
       ance and nitrogen availability: Growth of Skeletonema costatum in simulated upwelling conditions, Limnol. Oceanogr., 37, 989-1007,
       https://doi.org/10.4319/lo.1992.37.5.0989, 1992.

Smith, S. L., Yamanaka, Y., Pahlow, M., and Oschlies, A.: Optimal uptake kinetics: physiological acclimation explains the observed pattern
       of nitrate uptake by phytoplankton in the ocean, Mar. Ecol. Prog. Ser., 384, 1-12, https://doi.org/10.3354/meps08022, 2009.

590   Smith S. L., Yoshie, N, and Yamanaka, Y.: Physiological acclimation by phytoplankton explains observed changes in Si and N uptake rates
       during the SERIES iron-enrichment experiment. Deep-Sea Res. I, 57, 394-408, https://doi.org/10.1016/j.dsr.2009.09.009, 2010.

Smith, S. L., Pahlow, M., Merico, A., A.-Trejos, E., Sasai, Y., Yoshikawa, C., Sasaoka, K., Fujiki, T., Matsumoto, K., and Honda, M.
       C.: Flexible Phytoplankton Functional Type (FlexPFT) model: size-scaling of traits and optimal growth, J. Plankton Res., 38, 977-992,
       https://doi.org/10.1093/plankt/fbv038, 2016.

595   Tsujino, H., Urakawa, S., Nakano, H., Small, R. J., Kim, W. M., Yeager, S. G., Danabasoglu, G., Suzuki, T., Bamber, J. L., Bentsen, M.,
       Böning, C. W., Bozec, A., Chassignet, E. P., Curchitser, E., Dias, F. B., Durack, P. J., Griffes, S. M., Harada, Y., Ilicak, M., Josey, S. A.,
       Kobashi, C., Kobayashi, S., Komuro, Y., Large, W. G., Sommer, J. L., Marsland, S. J., Masina, S., Scheinert, M., Tomita, H., Valdivieso,
       M., and Yamazaki, D.: JRA-55 based surface dataset for driving ocean-sea-ice models (JRA55-do), Ocean Modelling, 130, 79-139,
       https://doi.org/10.1016/j.ocemod.2018.07.002, 2018.

600   Totterdell, I. J.: Description and evaluation of the Diat-HadOCC model v1.0: the ocean biogeochemical component of HadGEMS2-ES,
       Geosci. Model Dev., 12, 4497-4549, https://doi.org/10.5194/gmd-12-4497-2019, 2019.

Vichi, M., Pinardi, N., and Masina, S.: A generalized model of pelagic biogeochemistry for global ocean ecosystem, Part I: Theory, J. Mar. Syst., 64, 89-109, https://doi.org/10.1016/j.jmarsys.2006.03.006, 2007.

Ward, B. A., Dutkiewicz, S., and Follows, M. J.: Modelling spatial and temporal patters in size-structured marine planktonic communities: top-down and bottom-up controls, J. Plankton Res., 36, 31-47, https://doi.org/10.1093/plankt/fbt097, 2013.

605

Ward, B. A.: Assessing an efficient "Instant Acclimation" approximation of dynamic phytoplankton stoichiometry, J. Plankton Res., 39, 803-814, https://doi.org/10.1093/plankt/fbt040, 2017.
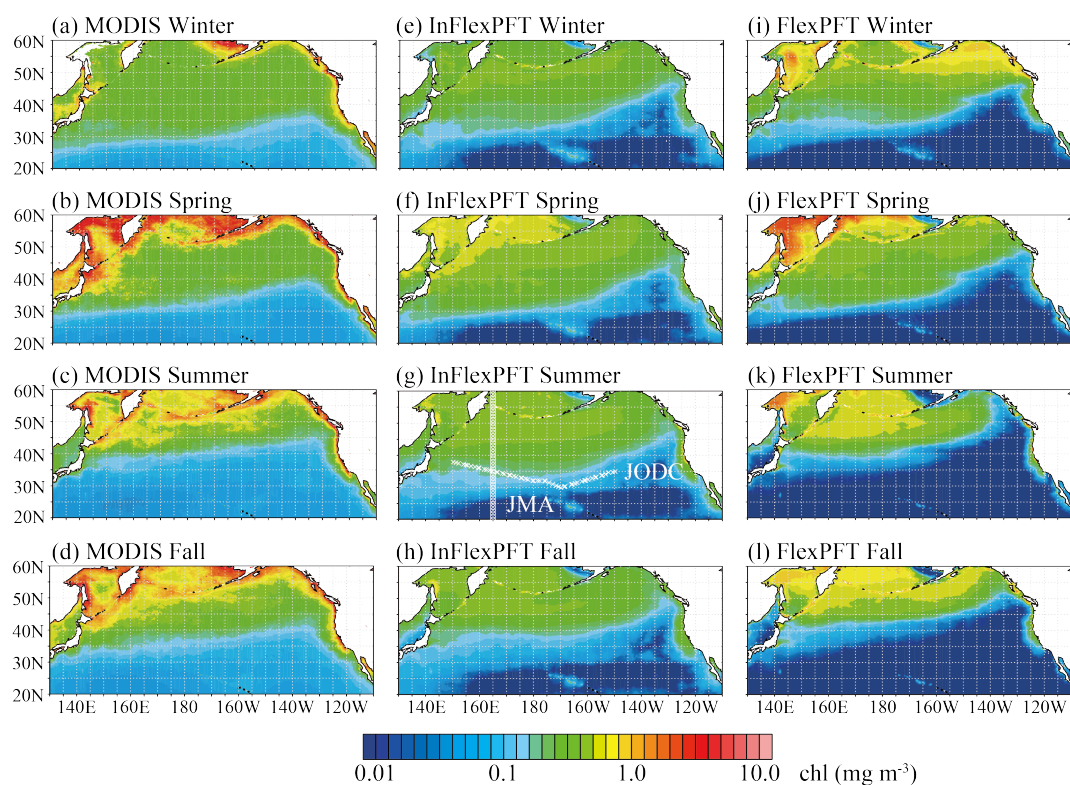
Figure 1. Climatological seasonal variations of surface Chl concentration (mg m^{-3}) from (a) - (d) MODIS-Aqua imagery and (e) - (l) two models. MODIS-Aqua imagery is averaged from 2003 to 2019 for each season. Two models are averaged from 2000 to 2019 for each season, and show an average of 20 m from the surface layer. White circles and crosses in Fig. 1g show two observation lines (the circles are the locations of the JMA data and the crosses are the locations of JODC data).
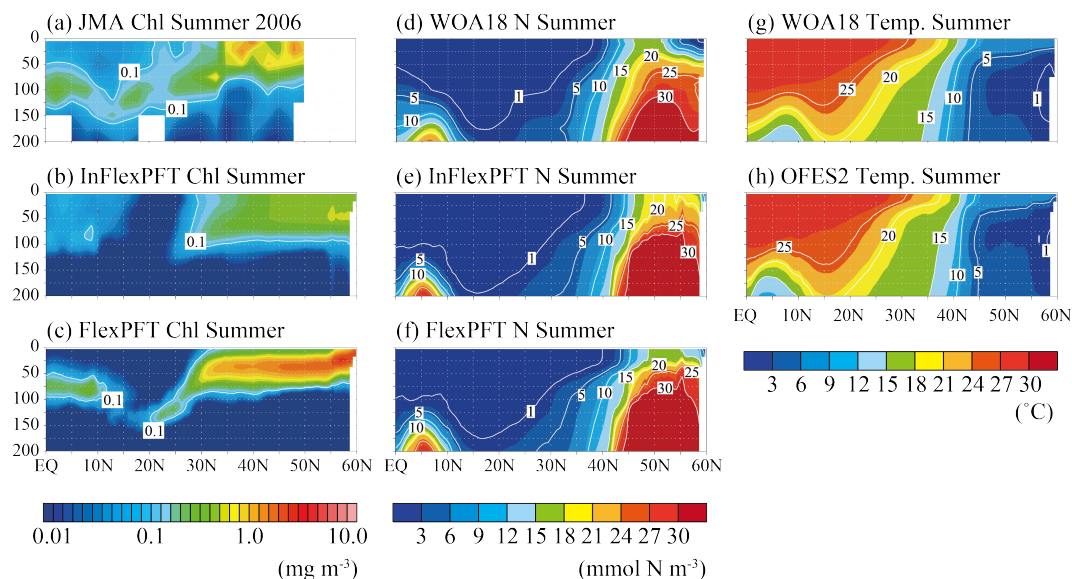
Figure 2. Comparison of vertical distributions of (a) - (c) summer (June, July and August) Chl concentration (mg m^{-3}), (d) - (f) summer N concentration (mmol N m^{-3}), and (g) - (h) summer T (°C) along 165°E (north-south section) in Fig. 1g (white circles). Fig. 2a shows in-situ observation data from the summer of 2006 by the JMA research vessel. Figs. 2d and 2g are from the climatological summer of WOA18. Figs. 2b, 2c, 2e, 2f, and 2h show the models' average value for the summer of 2000 to 2019.
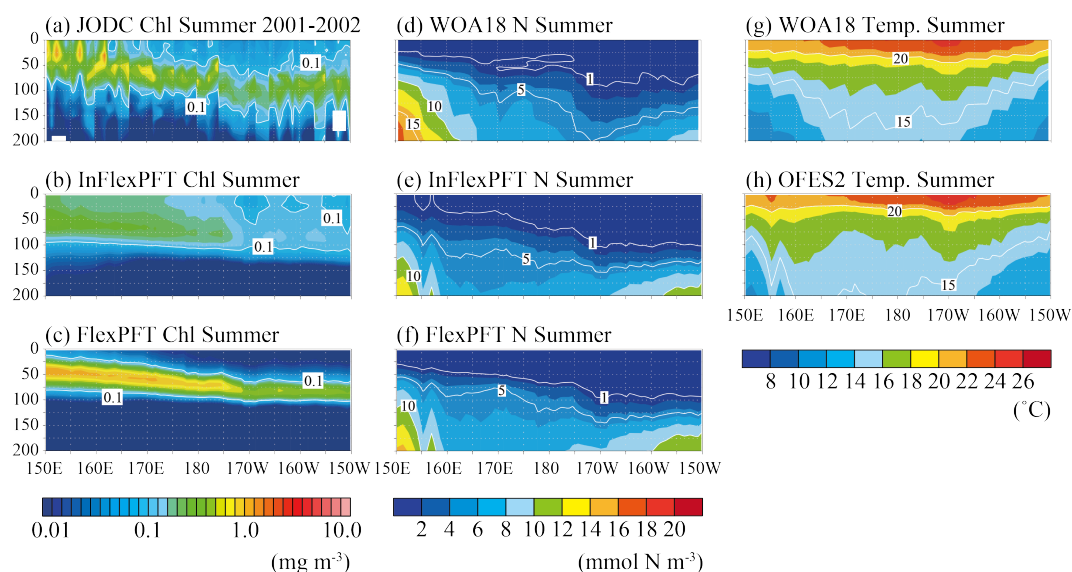
Figure 3. Same as for Fig. 2, but along the location of white crosses (east-west section) in Fig. 1g (white crosses). Fig. 3a shows in-situ observation data collected by the JODC in the summer of 2001-2002.
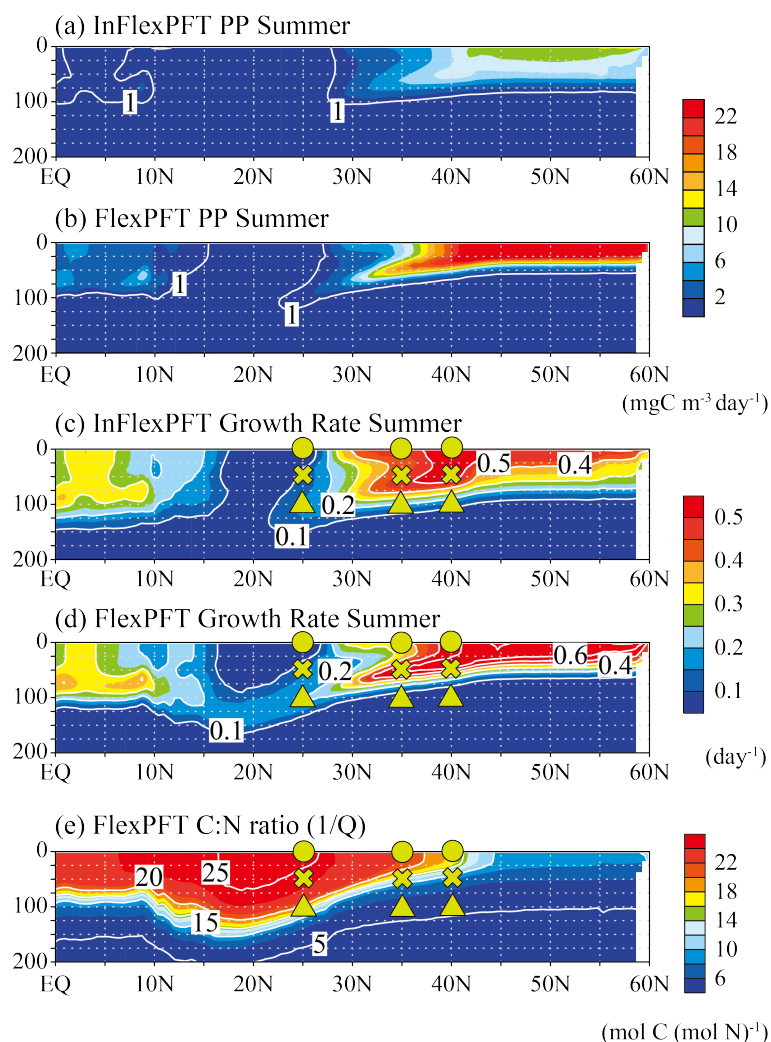
Figure 4. Comparison of vertical distributions of (a) - (b) summer primary production (mg C m^{-3} day^{-1}), and (c) - (d) summer phytoplankton growth rate (day^{-1}) between two models, and (e) vertical distribution of summer C:N ratio in the FlexPFT along 165°E (north-south section) in Fig. 1g (white circles). These figures show the average value for the summer of 2000 to 2019.
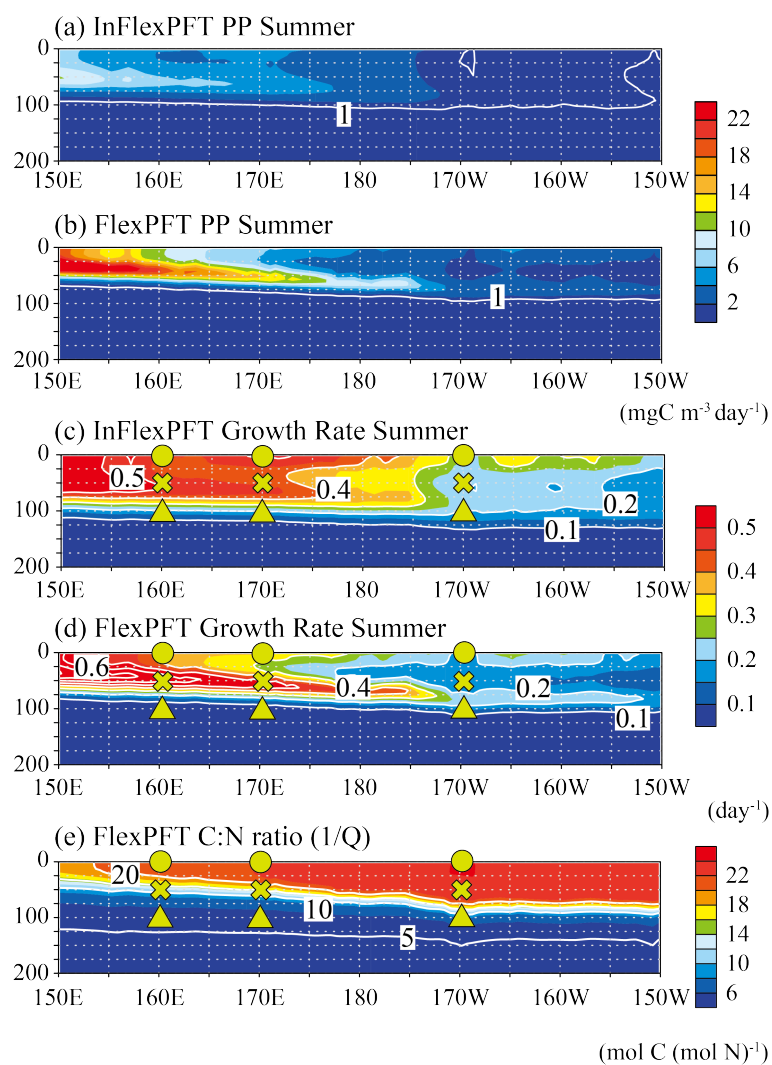
Figure 5. Same as for Fig. 4, but along the location of white crosses (east-west section) in Fig. 1g (white crosses).
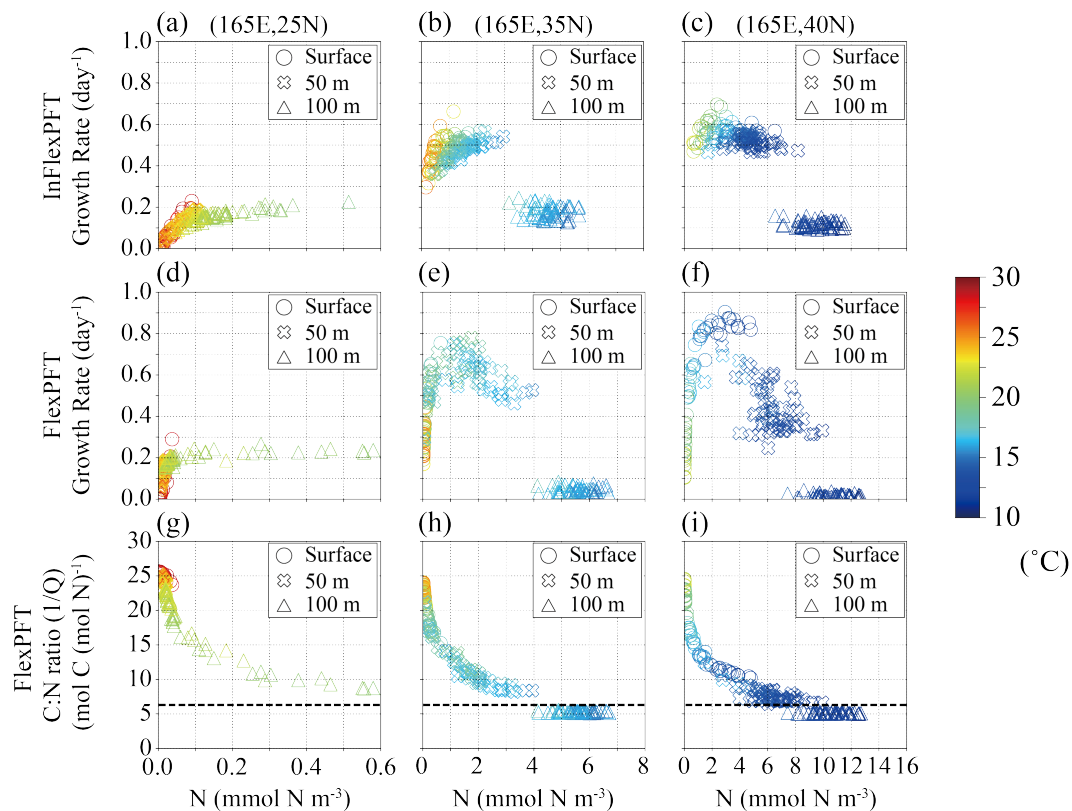
Figure 6. Monthly mean (a) - (f) phytoplankton growth rate (day^{-1}) in summer of 2000-2019 in Figs. 4c and 4d versus summer monthly mean N concentration (mmol N m^{-3}) in Figs. 2e and 2f for each depth (circle is surface, cross is 50 m depth, and triangle is 100 m depth in Figs. 4c and 4d) for each model, and summer monthly mean (g) - (i) C:N ratio versus summer monthly mean N concentration in Flex model. The color for each figure represent the summer monthly mean T ($^\circ$C) in Fig.2h. Dashed line in Figs. 6g, 6h, and 6i present constant C:N (106:16=6.625) ratio value.
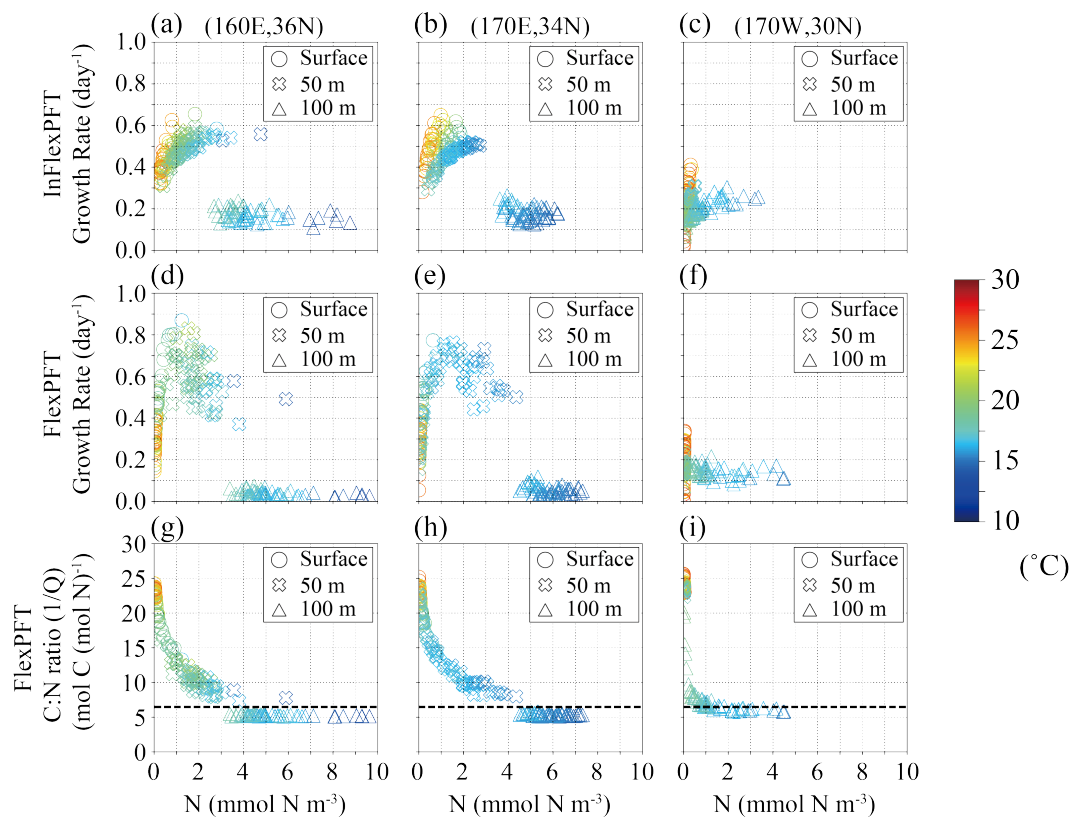
Figure 7. Monthly mean (a) - (f) growth rate (day^{-1}) in summer of 2000-2019 in Figs. 5c and 5d versus summer monthly mean N concentration (mmol N m^{-3}) in Figs. 3e and 3f for each depth (circle is surface, cross is 50 m depth, and triangle is 100 m depth in Figs. 5c and 5d) for each model, and summer monthly mean (g) - (i) C:N ratio versus summer monthly mean N concentration in the FlexPFT model. The color for each figure present summer monthly mean T (°C) in Fig. 3h. Dashed line in Figs. 7g, 7h, and 7i present constant C:N (106:16=6.625) ratio value.
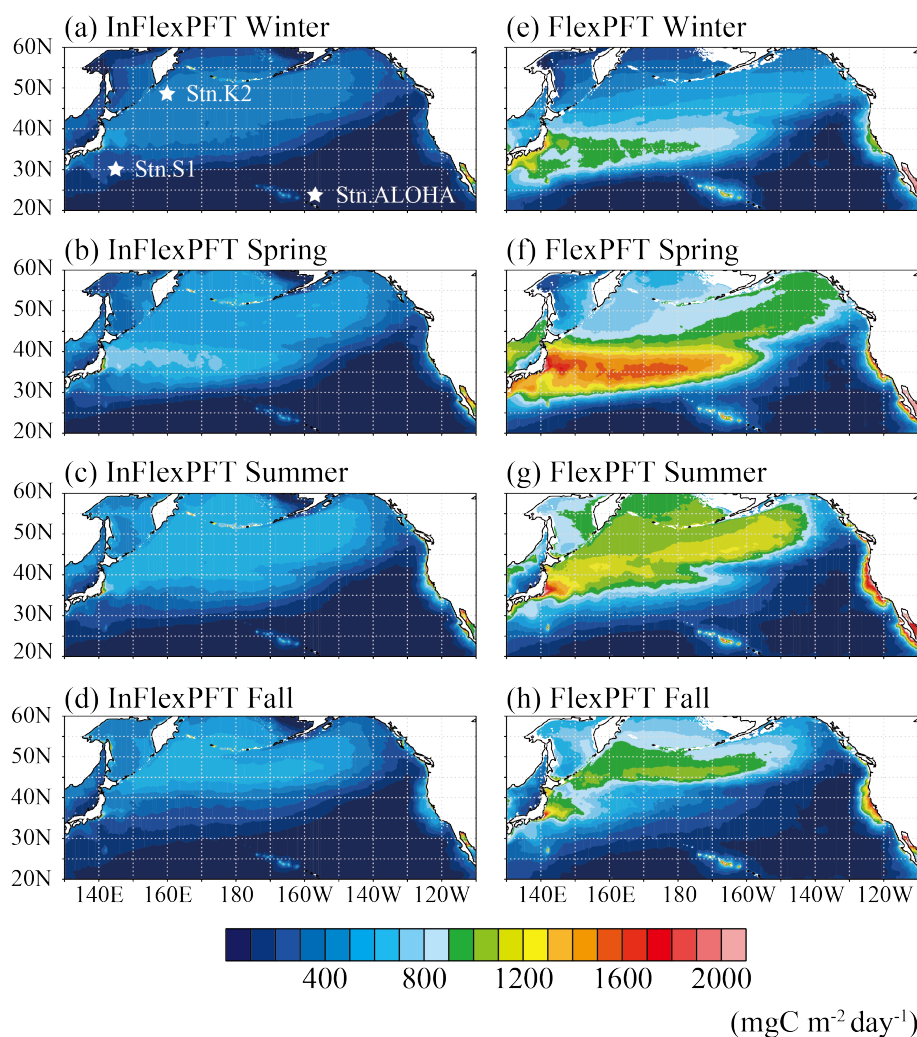
Figure 8. Climatological seasonal variations of vertical integrated (from surface to 100 m depth) primary production (mg C m^{-3} day^{-1}) from (a) - (d) the InFlexPFT, and (e) - (h) the FlexPFT. Two models are averaged from 2000 to 2019 for each season. Three stars in Fig. 8a show the observed stations.
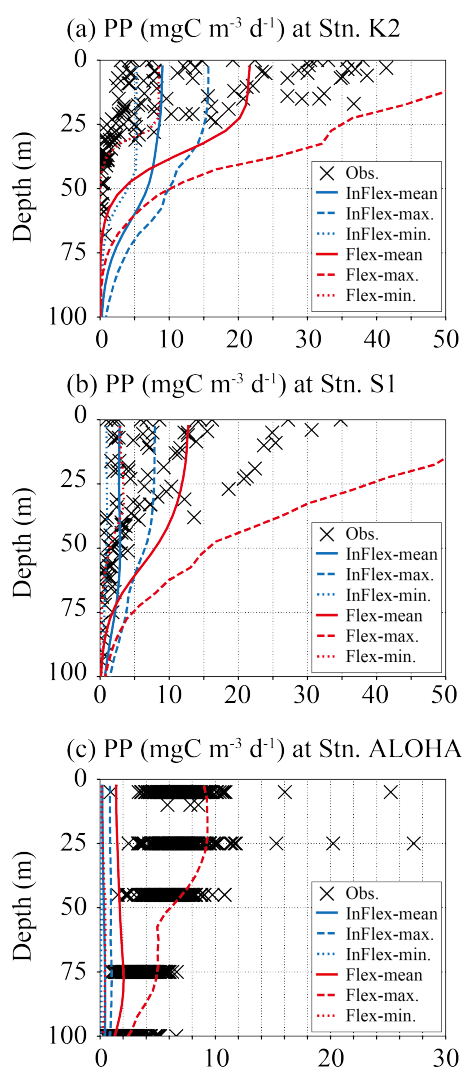
Figure 9. Comparison of vertical primary production (mg C m^{-3} day^{-1}) between observed station data and two models at (a) Station K2 (47°N,160°E), (b) Station S1 (30°N, 145°E), and (c) Station ALOAH (22.45°N, 158°W) in Fig. 8a. Observed Station K2 data is from 2010 to 2019, Station S1 is from 2010 to 2013, and Station ALOHA is from 2000 to 2019 (crosses). Two models show the mean primary production of 2000-2019 (solid line), the maximum of 2000-2019 (dashed line), and the minimum of 2000-2019 (dotted line). Blue lines are InFlexPFT and red lines are FlexPFT.

Table 1. Parameter of FlexPFT and InFlexPFT models

Parameter	Symbol	FlexPFT	InFlexPFT	Unit
Potential maximum growth rate	μ_{max}	2.2	1.5	day^{-1}
Chl-specific initial slop	α	2.0	2.0	No dim.
Potential maximum uptake rate for N	$\hat{V}_0$	1.0	1.0	day^{-1}
Potential maximum affinity for N	$\hat{A}_0$	1.0	2.0	m^3 (mmol N)$^{-1}$ day^{-1}